

Synthesis of a High-Capacity NiO/Ni Foam Anode for Advanced Lithium-Ion Batteries

Youngseok Song, Junesun Hwang, Sukyung Lee, Balamurugan Thirumalraj, Jae-Hun Kim, Péter Jenei, Jenő Gubicza,* and Heeman Choe

In recent years, lithium-ion batteries (LIBs) are used in a range of energy storage applications, such as mobile phones, electronic devices, and automobiles. Some recent research on LIBs has looked at replacing carbonaceous anode materials with transition metal oxides due to their high theoretical capacity, ranging from 500 to 1000 mAh g⁻¹. In particular, NiO is considered as one of the most promising options due to its high theoretical capacity (718 mAh g⁻¹). Herein, a porous NiO/Ni anode is fabricated via freezing/drying followed by thermal oxidation. The fabricated porous NiO/Ni anode is then characterized using X-ray diffraction scanning electron microscopy, and energy-dispersive X-ray spectroscopy. The cycling performance of the freeze-cast NiO/Ni anode is evaluated using a half-coin cell test, and it demonstrates superior electrochemical performance and good cycling stability during the charging/discharging process. The freeze-cast NiO/Ni anode also exhibits a higher rate performance when compared with that of commercial Ni foam and a conventional graphite anode. It is revealed that the initial crystalline surface oxide layer is amorphized, and the lattice defect density increases in the Ni struts during the lithiation process. However, these microstructure changes did not influence considerably the good electrochemical performance of the material.

consumer products and electric vehicles due to their high energy density, excellent cycle life, and affordable cost.^[1,2] However, despite their excellent stability during the cycling process, conventional graphite anodes used in LIBs are limited by their cycling capacity due to their inherently low theoretical capacity (372 mAh g⁻¹). Therefore, recent studies have focused on the development of high-capacity electrodes for LIBs to satisfy the current needs of consumers. As a result, a number of new anode materials have been proposed to achieve better cycling performance. In particular, transition metal oxides (e.g., Ni, Co, Fe, etc.) have received significant attention as high-capacity anodes for use in LIBs,^[3] with NiO receiving particular focus due to its high theoretical capacity (718 mAh g⁻¹), accessibility, and affordability. However, transition metal oxides still have a number of limitations that need to be overcome, such as low electronic conductivity, poor initial coulombic efficiency, and significant volume changes during charge/discharge, all of which eventually lead to

cycling instability and the loss of energy density.

To overcome these problems, porous or nanosized transition-metal oxide active materials can be used as LIB anodes to provide a larger surface area, a lower change in volume during the charge/discharge process, and shorter diffusion paths.^[4,5] To date, a variety of methods have been used for the synthesis of porous nanomaterials, including vapor deposition,^[6] dealloying,^[7] 3D printing,^[8] powder metallurgy,^[9] and freeze casting.^[10,11] Of these methods, freeze casting is most suited to the fabrication of materials with a large surface area and a sufficiently small pore size.^[12]


In this study, Ni foam was fabricated via freeze casting (hereafter, named Ni_{FC}), and an NiO/Ni_{FC} anode was produced via thermal oxidation. A commercially available Ni foam (hereafter, named Ni_C) was also prepared, and a NiO/Ni_C anode was produced via the same heat treatment. The generated NiO layer was used as the active material in the fabricated anode.^[13,14] The electrochemical performance of the NiO/Ni_{FC} anode was galvanostatically tested against a Li metal anode, and the changes in the microstructure and phase of the lithiated anode were tested during cycling.^[15] The phase composition and microstructural evolution of the NiO/Ni_{FC} anode after 50 cycles were investigated for both the strut interior and the surface oxide layer using scanning electron microscopy and X-ray analysis.

1. Introduction

In recent decades, there has been huge demand for high-capacity energy storage devices due to the increasing use of commercial electronic devices and electric vehicles. Lithium-ion batteries (LIBs) have been used for use in a wide range of electronic

Y. Song, J. Hwang, S. Lee, Dr. B. Thirumalraj, Prof. J.-H. Kim, Prof. H. Choe
School of Materials Science and Engineering
Kookmin University
77 Jeongneung-ro, Seongbuk-gu, Seoul 02707, Republic of Korea

Dr. P. Jenei, Prof. J. Gubicza
Department of Materials Physics
Eötvös Loránd University
P.O.B. 32, Budapest H-1518, Hungary
E-mail: jeno.gubicza@ttk.elte.hu

 The ORCID identification number(s) for the author(s) of this article can be found under <https://doi.org/10.1002/adem.202000351>.

© 2020 The Authors. Published by WILEY-VCH Verlag GmbH & Co. KGaA, Weinheim. This is an open access article under the terms of the Creative Commons Attribution-NonCommercial License, which permits use, distribution and reproduction in any medium, provided the original work is properly cited and is not used for commercial purposes.

DOI: 10.1002/adem.202000351

2. Results and Discussion

2.1. Material Analysis

The NiO/Ni_FC anode was fabricated by freeze casting followed by thermal oxidation. The as-prepared NiO/Ni_FC anode was then characterized using X-ray diffraction (XRD) analysis. For comparison, **Figure 1** shows the XRD patterns for commercially available Ni foam (NiO/Ni_C) and freeze-cast Ni foam (NiO/Ni_FC), both of which were thermally oxidized at 700 °C for 5 min. The diffraction patterns of both Ni foams show peaks corresponding to NiO (JCPDS 01-070-0989), indicating the successful formation of NiO on the Ni foam. No other diffraction peaks were observed, indicating that pure NiO was formed on the Ni foam without any other impurity phase.^[10,16]

The fabricated NiO/Ni_FC was further analyzed by field-emission scanning electron microscopy (FE-SEM). **Figure 2a,b** presents the FE-SEM images of the fabricated Ni foam both perpendicular and parallel to the freezing direction, respectively. The Ni foam (created from the water-solvent-based slurry, with the porosity of $p = \approx 75\%$) exhibited typical elongated and aligned microwalls with a measured thickness of 12 μm and micropores with a diameter of 15 μm (i.e., a lamellar architecture).^[11] Note that a Ni foam sample with the porosity of 75% was selected as a

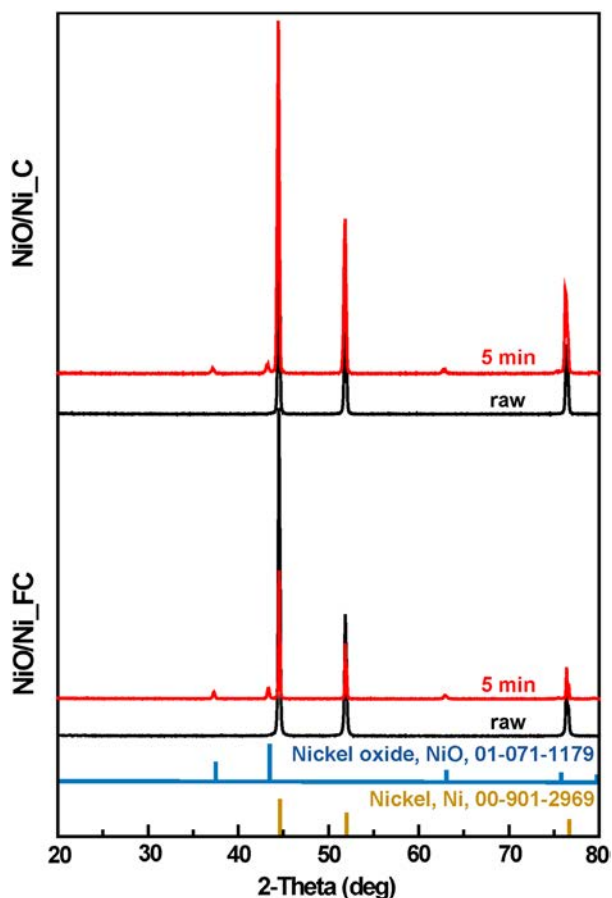


Figure 1. XRD patterns for NiO/Ni_C and NiO/Ni_FC thermally oxidized at 700 °C for 5 min in comparison with the standard peak for Ni (JCPDS #01-070-0989) and NiO (JCPDS #01-070-0989).

preliminary study owing to its reliable durability as a stand-alone electrode; however, it is desirable to increase the porosity up to above 85% to improve its electrochemical performance in a battery cell (enhanced surface area and active material filling amount if needed). The initial Ni foam (see **Figure 2a,b**) had a 3D porous structure with microscale pores distributed uniformly before the thermal oxidation process. The morphology of this pore architecture can be explained by the inherent characteristics of ice growth. During the freezing process, ice growth parallel to the thermal gradient occurs much faster than that perpendicular to the direction of the thermal gradient, resulting in the formation of lamellar ice-crystal walls aligned along the freezing direction.^[17] **Figure 2c,d** shows the surface images taken from the parallel view along the freezing direction before and after thermal oxidation at 700 °C for 5 min, respectively. It can be seen that the surface of the struts became rough due to oxidation.

Cross-sectional scanning electron microscopy (SEM) analysis and energy-dispersive X-ray spectroscopy (EDS) mapping were also carried out by measuring the thickness of the NiO layer and conducting elemental analysis of the NiO/Ni_FC. **Figure 3** displays the cross-sectional SEM and EDS mapping images for the NiO/Ni_FC thermally oxidized at 700 °C for 5 min. The SEM images clearly reveal that the entire surface of the porous Ni foam sample was successfully covered by the NiO layer following thermal oxidation at 700 °C for 5 min with a measured thickness of $0.48 \pm 0.15 \mu\text{m}$. EDS mapping also clearly indicates the formation of NiO layer on the Ni foam after thermal oxidation. These results suggest that the NiO layer was successfully formed on the Ni foam sample following 5 min of thermal oxidation. Note that the 5 min heat-treatment time was carefully selected for the NiO/Ni_FC anode with a maximum NiO thickness and decent NiO stability after comparing its morphology and microstructure with those of 10 and 15 min heat-treated Ni foam samples containing some occasional cracks and unstable morphology. Thinner NiO layers could be created by applying shorter heat treatment times than 5 min; however, the amount of NiO active material also decrease in that case, which then degrades the capacity of the NiO/Ni_FC anode.

2.2. Electrochemical Properties

Both the NiO/Ni_FC and NiO/Ni_C were tested and compared as the anode of a Li-ion coin cell battery using standard half-coin cell tests. Here, the NiO layer was considered as the active material for both the metal-foam anodes. The charge/discharge curves for the oxidized Ni foam anodes were obtained by cycling within a voltage window of 3.0–0.01 V at a constant current of 70 mA g^{-1} , as shown in **Figure 4a**. The capacity was estimated and compared between the two metal-foam anodes using the unit of specific capacity after being normalized by only the mass of the NiO active material for both the metal-foam anodes. The loading amount of the active material was determined as the mass change before and after the thermal oxidation treatment. Due to the differences in pore size, surface area, and porosity, the resultant NiO loading amount was different between the two metal-foam anodes (NiO in NiO/Ni_FC $\approx 0.0056 \text{ g}$ versus NiO in NiO/Ni_C $\approx 0.0033 \text{ g}$). The near double

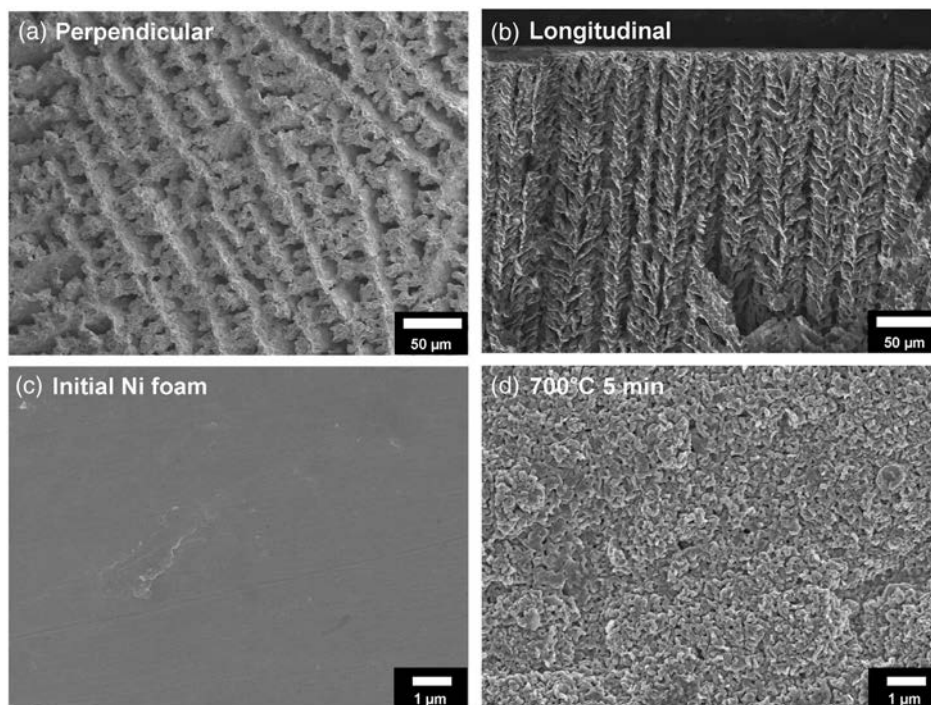


Figure 2. SEM images for freeze-cast Ni foam before thermal oxidation taken a) perpendicular and b) parallel to the freezing direction. c) Ni foam surface before thermal oxidation. d) Ni foam surface after thermal oxidation at 700 °C for 5 min.

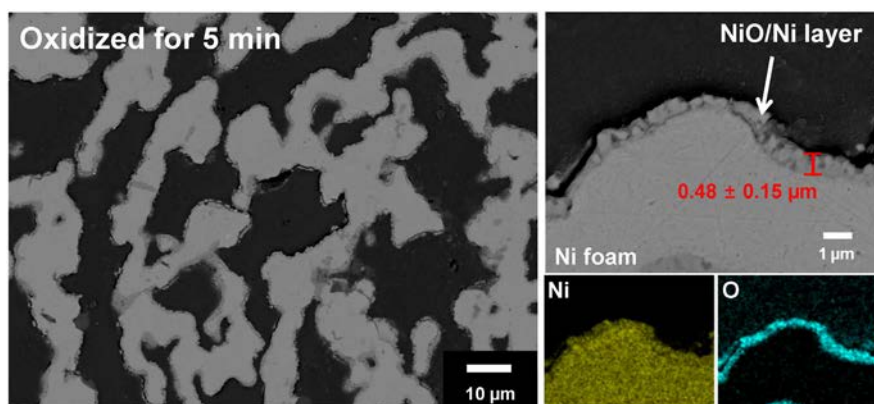


Figure 3. Cross-sectional SEM and EDS images for thermal oxidation time of 5 min.

loading amount with the NiO/Ni_{FC} anode, despite its lower porosity (75% versus 88%), suggests its considerably enhanced surface area due to the smaller pore size as compared with the NiO/Ni_C anode. Note that from Figure 4a, the first discharge curve exhibited a voltage plateau at around 0.6–0.7 V. The voltage plateau was then shifted in their subsequent second and tenth cycles to around 1.2–1.4 V that is mainly due to the formation of solid–electrolyte interface (SEI) resulting from electrochemically driven electrolyte degradation, which is a phenomenon also observed in other operating systems based on conversion reactions.^[18,19] The NiO/Ni_{FC} and NiO/Ni_C anode also reached a plateau at 2.1 V during charging, indicating the formation of NiO and the decomposition of Li₂O. The electrochemical

behavior of the NiO during the charge/discharge process is given as follows in Equation (1) and (2).^[14,20–22]

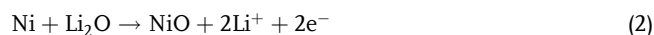
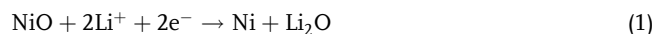


Figure 4b presents the cyclic performance of the oxidized Ni foam at a constant current of 70 mA g⁻¹ within a voltage window of 3.0–0.01 V. The initial discharge capacity of the NiO/Ni_{FC} anode (and the initial coulombic efficiency) was 861 mAh g⁻¹ (70.9%). In addition, the NiO/Ni_C anode (*p* = 88%, pore size 200 μm) with an oxidation time of 5 min had a discharge capacity

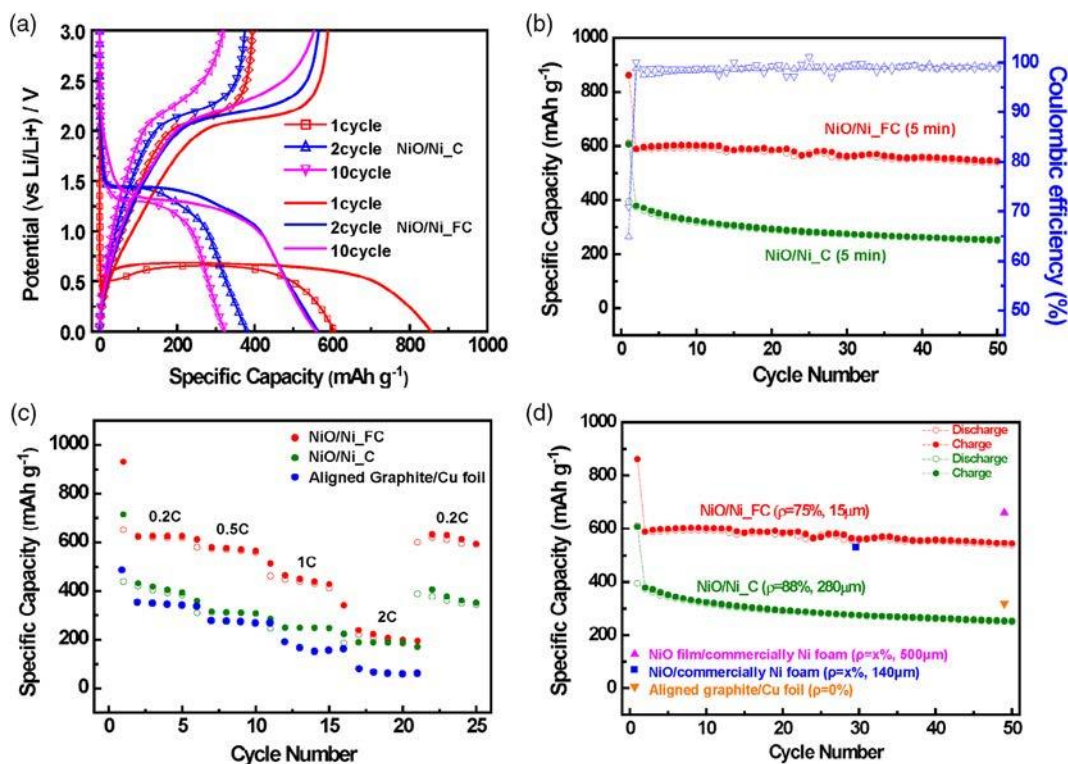


Figure 4. Electrochemical properties of the tested foams. a) Charge/discharge curves for the NiO/Ni_C and NiO/Ni_{FC}. b) Cycle performance of the NiO/Ni_{FC} and NiO/Ni_C at a current rate of 70 mAh g⁻¹ (≈0.1 C) over 50 cycles and their coulombic efficiency. c) Rate performance of the NiO/Ni_{FC} and NiO/Ni_C from 0.2 to 2 C. d) Comparison of the cycle performance of the NiO/Ni_{FC} and NiO/Ni_C with other anode materials.

of 607 mAh g⁻¹ and a reversible capacity of 394 mAh g⁻¹ (64.9%). This suggests that the cyclic performance of the NiO/Ni_{FC} is superior, with a higher coulombic efficiency, to the results reported by previous studies.^[14] Furthermore, the cycling performance of the NiO/Ni_{FC} electrode was more stable until the 50th cycle with a decent coulombic efficiency of 99.5%; in particular, the charge capacity of the NiO/Ni_{FC} electrode during the 50th cycle was 550 mAh g⁻¹.

Two important points are worth noting regarding the superior performance of the NiO/Ni_{FC}. First, under the same thermal oxidation conditions for the NiO/Ni_{FC} and NiO/Ni_C electrodes (i.e., 700 °C for 5 min), the NiO/Ni_{FC} exhibited a superior capacity of 590 mAh g⁻¹ without a noticeable decrease in capacity with an increasing number of cycles. The higher capacity and stability of the NiO/Ni_{FC} are due to the much smaller pore size and larger surface area than those of the NiO/Ni_C.^[23] Second, the Ni foam electrode synthesized in this study achieved excellent cyclic stability and high capacity without the addition of a binder or any other conductive material for the active material slurry, unlike a previous study.^[14] Based on these analyses, the NiO/Ni_{FC} has the potential to be used as a promising high-capacity anode material for LIBs.

The rate capability of the NiO/Ni_{FC} anode was analyzed by varying the C-rate from 0.2 to 2 C (Figure 4c). With an increasing C-rate, the discharge capacity was slightly reduced: 624, 580, and 448 mAh g⁻¹ for the rates of 0.2, 0.5, and 1 C, respectively. The obtained results were compared with those for the NiO/Ni_C

and a graphite anode (Figure 4c). The NiO/Ni_{FC} electrode exhibited a considerably higher capacity than the graphite anode at the highest C-rate (2 C).^[24] In addition, when switching back to 0.2 C, the NiO/Ni_{FC} electrode retained its original capacity of about 632 mAh g⁻¹, indicating high stability in the rate performance of the NiO/Ni_{FC} electrode due to the uniform arrangement of the microscale pores in the foam. To the best of our knowledge, this is the first study to demonstrate that a NiO layer grown on freeze-cast Ni foam can be used as a potential high-capacity anode for advanced LIBs. Here, it is important to note that this study focuses on the microporous Ni foam current collector design in conjunction with potential filling of active slurry material into its microscale pores, rather than the generally beneficial nanoporous current collector design due to its larger surface area and higher loading amount of active coating material. The use of a freeze-cast Ni foam current collector combined with a thermally grown NiO layer is thus a promising anode design, because it can provide a large surface area and a unique 3D electrode structure that can facilitate the transport of Li ions and accommodate volume expansion.^[3]

2.3. Comparison of the Phase Composition and the Microstructure Before and After Lithiation

To further understand the phase evolution and microstructure of the NiO/Ni_{FC} anode during lithiation, XRD and SEM analyses were performed after cycling. Figure 5 presents the X-ray

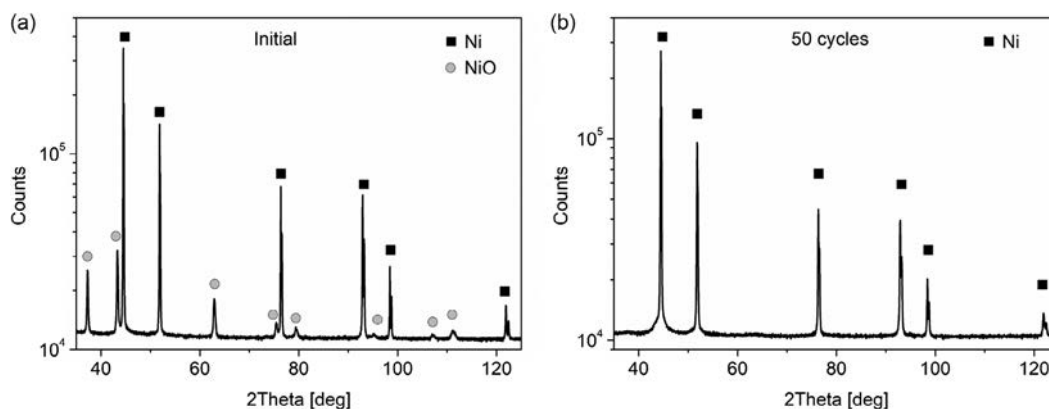


Figure 5. XRD patterns on a logarithmic intensity scale for the NiO/Ni_{FC} foam and the foam after 50 charge/discharge cycles.

diffractograms obtained for the NiO/Ni_{FC} anode before and after lithiation for 50 cycles. The NiO/Ni_{FC} exhibited a crystalline NiO phase in addition to the main Ni phase before lithiation (Figure 5a), indicating the successful formation of a NiO layer on the Ni foam during oxidation for 5 min. The fraction of NiO was 35 ± 5 wt%, which was calculated using the reference intensity ratio (RIR) with PDXL2 software. The crystalline peaks of the NiO phase disappeared after 50 charge/discharge cycles. This disappearance is likely due to the conversion of the NiO layer to an amorphous phase. A similar situation was observed for the Co anode used in our previously published report.^[15] In addition, the microstructure evaluation of the NiO/Ni_{FC} anode was further examined using the analysis Debye–Scherrer diffraction rings.

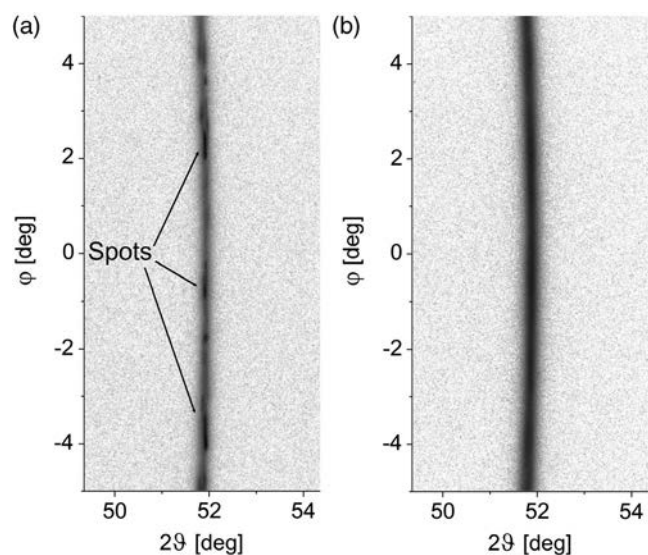


Figure 6. Debye–Scherrer diffraction rings for Ni reflection 200 a) of the NiO/Ni_{FC} foam and b) after 50 charge/discharge cycles.

were as narrow as the instrumental broadening ($\Delta(2\theta) \approx 0.03^\circ$), suggesting a lower dislocation density and twin-fault probability, as well as a larger crystallite size than the detection limit of the present diffraction setup (10^{13} m^{-2} for the dislocation density, 0.1% for the twin-fault probability, and $1 \mu\text{m}$ for the grain size). The coexistence of both sharp spots and continuous broad ring segments indicates that a heterogeneous Ni microstructure was produced in the initial foam.

The broader components of the Debye–Scherrer diffraction rings between the large intensity spots were also assessed using X-ray line profile analysis (XPLA). This portion of the microstructure had a relatively higher defect density, and the rings became more homogenous after 50 cycles. Therefore, the Debye–Scherrer diffraction rings were evaluated as a whole after 50 cycles. The microstructural parameters of the entire specimen sample were characterized using XPLA. Figure 7 shows the extended convolutional multiple whole profile (eCMWP) fitting analysis for the entire specimen sample after 50 cycles. The area-weighted mean crystallite size, dislocation density, and twin-fault probability were obtained from this analysis and are summarized in Table 1. In the as-received foam (before lithiation), within the

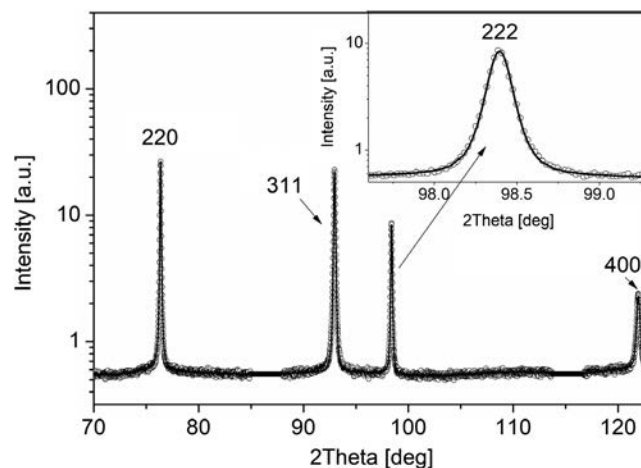


Figure 7. A section of the pattern fitted using the eCMWP method for the NiO/Ni_{FC} foam after 50 cycles. The open circles and the solid line represent the measured data and the fitted diffractograms, respectively.

Table 1. Microstructural parameters obtained from X-ray line profile analysis for the as-processed NiO/Ni₂C₂O₄ and the sample after 50 lithiation cycles. $\langle x \rangle_{\text{area}}$ is the area-weighted mean crystallite size, ρ is the dislocation density, and β is the twin-fault probability.

Sample	$\langle x \rangle_{\text{area}}$ [nm]	ρ [10^{14} [m] ⁻²]	β [%]
As-processed	1000<	<1.5	<0.1
After 50 cycles	450 ± 50	1.5 ± 0.2	0.3 ± 0.1

areas scattering the broader portions of the Debye–Scherrer rings, the crystallite size was about 1 μm (Table 1). As the spots in the Debye–Scherrer rings are scattered from volumes with a crystallite size larger than 1 μm, for the entire sample, the crystallite size of the main Ni phase was high (i.e., more than 1 μm). At the same time, the areas corresponding to the broader ring portions had a much higher dislocation density ($\approx 1.5 \times 10^{14} \text{ m}^{-2}$) than those volumes reflecting the sharp intensity spots ($< 10^{13} \text{ m}^{-2}$). Therefore, in the whole as-received sample, the average dislocation density was lower than the value of $\approx 1.5 \times 10^{14} \text{ m}^{-2}$ (see Table 1), because a significant proportion of the microstructure had a dislocation density lower than 10^{13} m^{-2} . The twin-fault probability in the as-received Ni foam was lower than the detection limit (0.1%). At the same time, the lithiation process resulted in a change in the microstructure of the Ni struts, which became more homogeneous with a lower crystallite size and a higher defect density (Table 1). For the entire lithiated sample, the average dislocation density was

$\approx 1.5 \times 10^{14} \text{ m}^{-2}$, whereas the twin-fault probability increased to $\approx 0.3\%$.

Following this, ex situ FE-SEM was also conducted for the microstructural analysis of the NiO/Ni₂C₂O₄ before and after cycling. **Figure 8a** presents the SEM images of the as-prepared NiO/Ni₂C₂O₄, showing a microscale pore structure with a relative density of about 26.8% and a porosity of 73.2%. The pore structure of the NiO/Ni₂C₂O₄ after lithiation is displayed in **Figure 8b**. A significant change in the morphology and pore size of the NiO/Ni₂C₂O₄ can be clearly observed. This change in morphology might be due to the conversion of crystalline oxide to an amorphous form. Therefore, the disappearance of the crystalline peaks for the NiO layer in the XRD patterns (Figure 5) may have been due to changes into the amorphous form of NiO during lithiation. In addition, EDS measurements were carried out with an electron energy of 5 keV for the NiO/Ni₂C₂O₄ before cycling. The penetration depth of the electrons for the NiO was about 0.2 μm as estimated from the density of the oxide phase (6.67 g cm^{-3}). The oxygen concentration of the NiO layer was $\approx 55 \text{ at}\%$. In addition, the penetration depth of the electrons for the NiO and Ni phases was about 1.5 μm with an energy of 20 keV. The oxygen concentration of the NiO/Ni₂C₂O₄ was about 37–43 at% at a higher electron energy of 20 keV. This concentration range was obtained from measurements taken at different locations on the surface. The measured oxygen concentration is lower than $\approx 50\%$, which is characteristic for NiO; therefore, the surface layer studied by 20 keV electrons contains Ni besides NiO, i.e., the thickness of the NiO layer is smaller

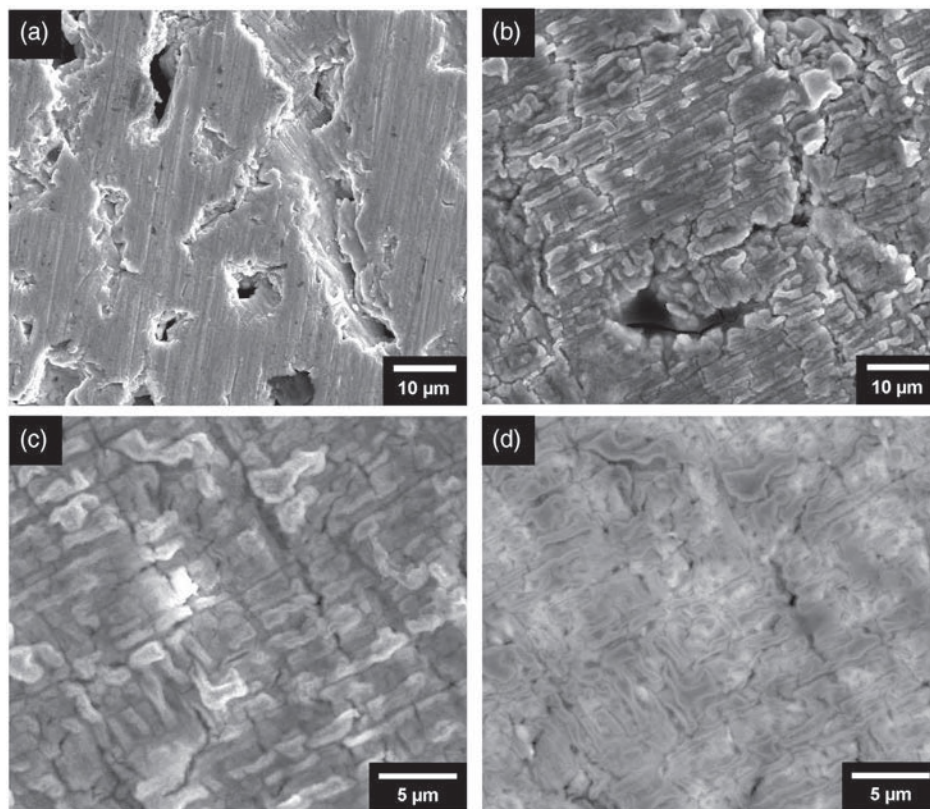


Figure 8. SEM images obtained for a) the as-processed NiO/Ni₂C₂O₄ and b–d) after 50 lithiation cycles.

Table 2. The oxygen concentration measured using EDS at electron energies of 5 and 20 keV for the as-processed NiO/Ni₂C and the sample after 50 lithiation cycles.

Electron energy [keV]	As-processed		After 50 cycles	
	5	20	5	20
Oxygen concentration [at%]	55	37–43	58–77	44–63

than 1.5 μm . Based on these measurements, the thickness of the oxide layer was estimated to be between 0.2 and 1.5 μm on the Ni foam surface, which is in accordance with the SEM/EDS observations (see Figure 3a), which indicate the thickness of $\approx 0.48 \mu\text{m}$.

Furthermore, EDS measurements of the NiO/Ni₂C were carried out after 50 cycles. The EDS detected a significant amount of oxygen on the NiO/Ni₂C after 50 cycles, as summarized in Table 2. The experimental error of the concentration values was 1 at%. The oxygen content was measured with the electron energies of 5 and 20 keV. The EDS analysis revealed that the oxygen levels of NiO/Ni₂C were in the ranges of 58–77 at% and 44–63 at%, for 5 and 20 keV, respectively. The obtained values were much higher than the oxygen content of the as-prepared NiO/Ni₂C sample before cycling. The higher levels of oxygen in the NiO/Ni₂C might be due to the phase change of the crystalline oxide phase to an amorphous form after cycling. In addition, the fragmentation of the surface layer was analyzed using SEM during cycling. The surface oxide layer was fragmented into scutes, as shown in Figure 8c. In the vCD image presented in Figure 8d, the bright border area of the scutes suggests that the surface was covered by a light element-rich (e.g., Li and/or O) layer with a thickness of about 200 nm.^[15,25,26]

This study suggests the fragmentation and amorphization of the surface oxide layer during lithiation and a simultaneous refinement of the microstructure and an increase in the defect density in the Ni struts under the surface layer. These observations may have a common origin, namely, the effect of stresses developed in the surface NiO layer due to the volume change during charging/discharging. It is worth noting that although oxide amorphization was also observed for Co anode, the strut microstructure remained practically unchanged.^[15] As Co is harder than Ni, the stresses in the surface layer might have caused less plastic deformation in Co during lithiation as compared with Ni.

3. Conclusion

In this work, Ni foam was successfully prepared via freeze-cast. A uniform NiO layer was grown on the Ni foam surface using thermal oxidation at 700 °C for 5 min (NiO/Ni₂C). The NiO/Ni₂C was then used as an anode for an LIB and tested using a half-coin cell test. The integrated NiO/Ni₂C anode exhibited good cycling performance with an initial discharge capacity and a coulombic efficiency of 861 mAh g⁻¹ and 70.9%, respectively. In addition, the NiO/Ni₂C anode had remarkably stable capacity retention and a comparatively high capacity (550 mAh g⁻¹) after 50 cycles due to its large surface area

and uniform nanopores. Given its expected low processing costs, the proposed NiO/Ni₂C represents a promising candidate as an anode for high-capacity LIBs. Ex situ XRD and SEM analyses were also performed before and after the cycling of the NiO/Ni₂C anode, finding that the crystalline nature of the oxide layer was converted into an amorphous form after lithiation, with additional refinement of the microstructure and increasing defect density in the Ni struts under the surface layer. Despite these microstructural changes, the NiO/Ni₂C exhibited good electrochemical performance even after 50 cycles of lithiation.

4. Experimental Section

Preparation of the Ni Foam Electrode: The NiO/Ni₂C anode was fabricated via freeze-cast followed by thermal oxidation. First, a metal precursor slurry was prepared by dissolving NiO powder (0.1–5 μm , Inframat Advanced Materials, USA) and a polyvinyl alcohol (PVA) binder (a molecular weight of 89 000–98 000 g mol⁻¹, Sigma-Aldrich, USA) in deionized water with dispersant (Darvan 811, Vanderbilt Co, USA). The slurry was then agitated with a magnetic stirrer for 30 min and sonicated for 1 h at room temperature. This process was carried out twice to prevent the agglomeration of particles. Subsequently, the slurry was poured into a cylindrical Teflon-insulated Cu rod submerged in liquid nitrogen within a stainless-steel bowl. The Cu rod was cooled at -10 °C using a temperature-controlled heating band to freeze the slurry with the top slurry surface being cooled at the rate of $\approx 0.4 \text{ }^\circ\text{C min}^{-1}$. The frozen ice slurry (referred to as the ice-templated green body) was taken out of the mold and sublimed in a freeze dryer (FDU-7003, Operon, Republic of Korea) at -80 °C and under a residual pressure of 0.009 Torr for 48 h. During this process, pores were created in and on the green body by removing the ice that had formed. The porous green body was then sintered in a tube furnace under a mixed Ar (5%) and H₂ gas atmosphere. Preliminary heat treatment was carried out at 300 °C for 4 h to reduce the oxide to its metal form and to remove the binder, followed by sintering at 1000 °C for 3 h with a heating and cooling rate of 5 and 3 °C min⁻¹, respectively.^[10,27]

Fabrication of a Stand-Alone Ni Foam Anode: The synthesized Ni foam (V5: 5 vol% NiO, -10 °C) was cut into a CR2032 coin cell sample with a thickness of $\approx 400 \mu\text{m}$. Note that for the assembly of the half coin cell, a thickness of $\approx 400 \mu\text{m}$ was chosen, as it was the maximum thickness allowed with the highest capacity for a stand-alone single Ni foam electrode. To grow the Ni oxide layer on the surface of the Ni foam coin sample, the Ni foam sample was heat-treated at 700 °C for different times between 5 and 15 min in an electric furnace in air.^[13] The best electrochemical performance was achieved for the oxidation time of 5 min; therefore, the results obtained only for this material are shown in this study. To examine the effect of the porous architecture on subsequent electrochemical performance, a commercially available Ni foam anode was also prepared using the same oxidation conditions for comparison (700 °C, 5 min).^[14]

Characterization of the Freeze-Cast Material: The NiO/Ni₂C and NiO/Ni₂C anode was studied using XRD patterns (Rigaku, D-MAX2500, Japan, CuK α radiation in a 2 θ range from 20° to 80°). The microstructure of the NiO/Ni₂C was imaged using optical microscopy (OM; Olympus, PME 3, Japan), FE-SEM (JEOL, JSM-7610 F, Japan), and EDS. For EDS, an Apollo XP 10 mm² silicon drift detector (SDD) mounted at a distance of 62 mm from the intersection point and a Genesis v6.42 analytical software were used, both manufactured by Ametek EDAX. The calculation method of the element concentrations was a so-called ZAF Quantification, Standard-less Element Normalized procedure (ZAF: corrections for atomic number effects (Z), absorption (A), and fluorescence (F) were calculated on the basis of physical models). Based on the temporal stability of the SDD, our setup was not calibrated for the specific measurement run of samples. The elemental sensitivities were set earlier using stoichiometric oxide samples of iron group elements. The following exposure settings were applied: a working distance of 10 mm, the

excitation voltages of 5 and 20 kV, and a beam current of 4 nA. The obtained count rate was 4000–10 000 cps. A total count of around one million was typically collected, resulting in 1% relative statistical accuracy of element concentrations. The porosity of the NiO/Ni₂C₂O₄ electrode was calculated by considering the theoretical density of bulk Ni (8.908 g cm⁻³) and by measuring its mass and volume based on the height and diameter of the NiO/Ni₂C₂O₄ electrode. The microstructure of the Ni foam disks was studied with cross-sectional cut perpendicular to the freezing direction using SEM.

Electrochemical Tests for the NiO/Ni₂C₂O₄ Anode: The electrochemical performance of the NiO/Ni₂C₂O₄ anode was evaluated using standard Li half-cell tests. The cell was assembled in an Ar-filled glove box. A CR2032 coin-type cell was used for coin-cell assembly. The NiO/Ni₂C₂O₄ anode was used as the working electrode with a diameter of 11 mm and a thickness of 400 μm, and Li foil was used as both the counter and reference electrodes. A porous polypropylene membrane (Asahi Kasei Chemicals) was used as a separator, and 1 M LiPF₆ containing ethylene carbonate/diethylene carbonate (EC:DEC; 3:7 vol%, PANAX Etec) was used as the electrolyte. The cells were tested within a voltage window of 3.0 and 0.01 V versus Li⁺/Li at a constant current of 70 mA g⁻¹ at 25 °C using a battery testing system (CTS-Lab, BaSyTec, Germany).

Study of the Effect of Lithiation on the NiO/Ni₂C₂O₄ Anode by XRD: The microstructure of the NiO/Ni₂C₂O₄ anode was characterized using XRD before and after 50 cycles of lithiation. The change of the phase composition of the NiO/Ni₂C₂O₄ anode during lithiation was examined using a Rigaku Smartlab X-ray diffractometer and Bragg–Brentano geometry with a 1D D/Tex detector (using CuKα radiation). Diffractograms of the samples were evaluated with the PDXL2 program using the ICDD-2018 database. In addition, the microstructure of the NiO/Ni₂C₂O₄ anode was assessed with XLPD during the charging/discharging process using a high-resolution rotating anode diffractometer (RA-MultiMax9, Rigaku) with CuKα₁ (λ = 0.15406 nm) radiation. The line profiles were determined from the intensity distribution perpendicular to the Debye–Scherrer rings obtained from the integrated 2D intensity distribution along the rings. The line profiles were analyzed using the eCMWP fitting method.^[28,29] In this approach, the diffraction pattern was fitted to the sum of a background spline and the convolution of the instrumental patterns and the theoretical line profiles related to the dislocations, crystallite size, and twin faults. The instrumental pattern was measured on a LaB₆ line profile standard material. The area-weighted mean crystallite size ($\langle x \rangle_{\text{area}}$), the dislocation density (ρ), and the twin-fault probability (β) were determined from this analysis. The area-weighted mean crystallite size was calculated from the median and the variance of the crystallite size distribution: $\langle x \rangle_{\text{area}} = m \cdot \exp(2.5\sigma^2)$. The twin-fault probability corresponds to the relative frequency of the twin-faults among the {111} lattice planes.

Acknowledgements

This research was supported by the Korea Electric Power Corporation (Grant No.: R18XA06-41). J.G. and P.J. would like to acknowledge supports from the János Bolyai Research Scholarship of the Hungarian Academy of Sciences and the Ministry for Innovation and Technology of Hungary (ÚNKP-19-4, No. 2018-2.1.17-TÉT-KR-2018-00003).

Conflict of Interest

The authors declare no conflict of interest.

Keywords

anode, lithiation, metal foam, nickel, porous

Received: March 25, 2020

Revised: May 26, 2020

Published online: June 21, 2020

- [1] P. Poizot, S. Laruelle, S. Grugeon, L. Dupont, J. M. Tarascon, *Nature* **2000**, *407*, 496.
- [2] V. Etacheri, R. Marom, R. Elazari, G. Salitra, D. Aurbach, *Energy Environ. Sci.* **2011**, *4*, 3243.
- [3] H. Park, H. Choi, K. Nam, S. Lee, J. H. Um, K. Kim, J. H. Kim, W. S. Yoon, H. Choe, *J. Electron. Mater.* **2017**, *46*, 3789.
- [4] L. Ji, Z. Lin, M. Alcoutlabi, X. Zhang, *Energy Environ. Sci.* **2011**, *4*, 2682.
- [5] J. Jiang, Y. Li, J. Liu, X. Huang, C. Yuan, X. W. Lou, *Adv. Mater.* **2012**, *24*, 5166.
- [6] V. Poserin, S. Marcuson, J. Shu, D. S. Wilkinson, *Adv. Eng. Mater.* **2004**, *6*, 454.
- [7] L. Sun, C. L. Chien, P. C. Seanson, *Chem. Mater.* **2004**, *16*, 3125.
- [8] A. E. Jakus, S. L. Taylor, N. R. Geisendorfer, D. C. Dunand, R. N. Shah, *Adv. Funct. Mater.* **2015**, *25*, 6985.
- [9] G. Walther, B. Klöden, T. Büttner, T. Weissgärber, B. Kieback, A. Böhm, D. Naumann, S. Soberi, L. Timberg, *Adv. Eng. Mater.* **2008**, *10*, 803.
- [10] H. Jo, M. J. Kim, H. Choi, Y.-E. Sung, H. Choe, D. C. Dunand, *Metall. Mater. Trans. E* **2016**, *3*, 46.
- [11] S. Lee, J. Tam, W. Li, B. Yu, H. J. Cho, J. Samei, D. S. Wilkinson, H. Choe, U. Erb, *Mater. Charact.* **2019**, *158*, 109939.
- [12] W. L. Li, K. Lu, J. Y. Walz, *Int. Mater. Rev.* **2012**, *57*, 37.
- [13] L. De Los Santos Valladares, A. Ionescu, S. Holmes, C. H. W. Barnes, A. Bustamante Domínguez, O. Avalos Quispe, J. C. González, S. Milana, M. Barbone, A. C. Ferrari, H. Ramos, Y. Majima, *J. Vac. Sci. Technol. B, Nanotechnol. Microelectron. Mater. Process. Meas. Phenom.* **2014**, *32*, 051808.
- [14] C. Wang, D. Wang, Q. Wang, H. Chen, *J. Power Sources* **2010**, *195*, 7432.
- [15] J. Gubicza, R. Németh, H. Park, K. Kim, J. H. Kim, M. Óvári, M. Mohai, H. Choe, *Adv. Eng. Mater.* **2018**, *20*, 1.
- [16] B. Janković, B. Adnadević, S. Mentus, *Chem. Eng. Sci.* **2008**, *63*, 567.
- [17] S. Deville, E. Saiz, A. P. Tomsia, *Acta Mater.* **2007**, *55*, 1965.
- [18] X. H. Huang, J. P. Tu, C. Q. Zhang, F. Zhou, *Electrochim. Acta* **2010**, *55*, 8981.
- [19] X. Li, A. Dhanabalan, C. Wang, *J. Power Sources* **2011**, *196*, 9625.
- [20] M. Y. Cheng, Y. S. Ye, T. M. Chiu, C. J. Pan, B. J. Hwang, *J. Power Sources* **2014**, *253*, 27.
- [21] X. Wang, X. Li, X. Sun, F. Li, Q. Liu, Q. Wang, D. He, *J. Mater. Chem.* **2011**, *21*, 3571.
- [22] X. Li, A. Dhanabalan, K. Bechtold, C. Wang, *Electrochem. Commun.* **2010**, *12*, 1222.
- [23] L. P. Lefebvre, J. Banhart, D. C. Dunand, *Adv. Eng. Mater.* **2008**, *10*, 775.
- [24] J. Billaud, F. Bouville, T. Magrini, C. Villeveille, A. R. Studart, *Nat. Energy* **2016**, *1*, 1.
- [25] S. Ni, T. Li, X. Lv, X. Yang, L. Zhang, *Electrochim. Acta* **2013**, *91*, 267.
- [26] J. Vetter, P. Novák, M. R. Wagner, C. Veit, K. C. Möller, J. O. Besenhard, M. Winter, M. Wohlfahrt-Mehrens, C. Vogler, A. Hammouche, *J. Power Sources* **2005**, *147*, 269.
- [27] S. Sánchez-Salcedo, J. Werner, M. Vallet-Regí, *Acta Biomater.* **2008**, *4*, 913.
- [28] G. Ribárik, J. Gubicza, T. Ungár, *Mater. Sci. Eng. A* **2004**, *387–389*, 343.
- [29] L. Balogh, G. Ribárik, T. Ungár, *J. Appl. Phys.* **2006**, *100*, 023512.